Heliyon 9 (2023) e17143

Contents lists available at ScienceDirect

Heliyon

journal homepage: www.cell.com/heliyon

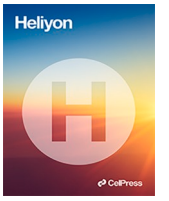

Flattened Gaussian focal spot with uniform phase produced by photon sieve

Changjie Cheng *, Qing Cao **, Lihua Bai, Chaoyue Li, Jirui Zhu

Department of Physics, Shanghai University, Shanghai, 200444, China

ARTICLE INFO

Keywords:
Photon sieve
Flattened Gaussian beam
Equivalent pupil function

ABSTRACT

The equivalent pupil and the point spread function constitute the Fourier–Bessel transform relation. Based on this, we established the equivalent pupil function theory of rotating symmetric photon sieve and derived the Fourier transform of the flattened Gaussian function. The focal spot produced by this type of photon sieve exhibits a uniform intensity and phase distribution. According to the numerical results, the flattened Gaussian field distribution is consistent with the designed function. In addition, the nonuniformity in intensity and phase is approximately 1% and less than 1/170 wavelength, respectively.

1. Introduction

Uniform illumination has been used in various fields of optics. For microscopy in the visible spectrum, Köhler illumination which provides uniform illumination plays an important role [1]. Besides microscopy [2,3], uniform illumination has also been applicated in fields such as lithography [4], inertial confinement fusion [5], laser processing [6], compact antenna test range [7], and so on [8]. The flattened Gaussian beam which has a flat-top spatial profile was introduced by Gori [9]. This flat-top beam provides one kind of interesting possibility for uniform illumination. Several theoretical and experimental studies for flattened Gaussian beams were carried out by different groups [4,10–12]. Similarly, super-Gaussian beams [13] and infinite Laguerre Gaussian modes [14] can also have flat-top profiles. But because of the more complicated mathematics, we do not adopt these two models. Herein, we propose a specific photon sieve that produces a flattened Gaussian focal spot with uniform intensity and a uniform phase.

Photon sieve was proposed by Kipp et al. [15], and the original idea was that the pinhole radius could break through the width limit of the outermost zone plate ring and enhance the resolution by improving the characteristic size of the element. In subsequent studies, researchers have realized that the photon sieve structure offers a greater degree of freedom of design that can be utilized for achieving completely new functions. Such as the fractal photon sieve which provides higher resolution [16], the spiral photon sieve which can modulate phase [17], the binary photon sieve aiming at promoting efficiency [18], the wavefront coding photon sieve expanding the bandwidth [19], the random photon sieve that suppresses higher-order focal points [20], and so on. As a result, photon sieve has been studied for telescopes [21–23], beam shaping [17,24], imaging [19,25], holograms [26,27], and biological optics [28].

For a deeper understanding of the photon sieve, paraxial and non-paraxial analytical expressions of the photon sieve were obtained by the Rayleigh–Sommerfeld integral [29,30]. The influence of the pinholes' shape, which indicated the importance of the pinhole area, was sequentially discussed by researchers as well [31–34]. Large apertures or high numerical aperture photon sieves may contain

* Corresponding author.
** Corresponding author.
E-mail addresses: cjcheng@shu.edu.cn (C. Cheng), qcao@shu.edu.cn (Q. Cao).

https://doi.org/10.1016/j.heliyon.2023.e17143
Received 9 August 2022; Received in revised form 2 June 2023; Accepted 8 June 2023
Available online 9 June 2023

millions or even hundreds of millions of pinholes that cause considerable inconvenience to simulation and optimization. To solve this drawback, the pinhole ring model for photon sieve was proposed [35,36]. In this model, all pinholes in the same ring are considered together instead of calculating them individually.

Some photon sieve models rely on a particular arrangement of pinholes [16,37]. The apodized photon sieves also need to adjust the distribution of pinholes [38–42]. Based on the pinhole ring model and equivalent pupil function theory working on zone plate [43,44], we further develop the equivalent pupil function theory of rotational symmetric photon sieve. In this theory, the single ring described by the pinhole ring model is extended to the whole photon sieve plane; consequently, the distribution function of the optical field passing through the rotating symmetric photon sieve is analytically related to the function of the optical field in the focal plane. A detailed derivation is presented in Section 2. Since this theory is based on scalar diffraction theory, the proposed photon sieve is polarization independent. Also, this theory is based on the rotational symmetric in every ring, it can be applied in an aperiodic photon sieve, but there may exist higher-order focal points that can be suppressed by random photon sieve [20].

In Section 3, we present the mathematical derivation that converts plane waves into flattened Gaussian beams with a uniform phase. For an arbitrary optical element, the pupil function exhibits a Fourier transform relation with the point spread function in the focal plane. As the transformation relation is reversible, we can design the optical field distribution function in the focal plane in advance, use the equivalent pupil function theory to calculate the pupil function of the photon sieve, and determine the pinhole distribution.

In Section 4, we numerically simulate the distribution of the optical field in the focal plane of the designed photon sieve. The results reveal a highly uniform intensity and uniform phase in the center of the focal spot. We test the equivalent pupil function model as well, which was compatible with the sum of the pinhole model. In Section 5, we summarize the study. We believe that the work presented in this paper will enlighten the design of photon sieve for relevant fields.

2. Equivalent pupil function theory

As displayed in the schematic of the photon sieve in Fig. 1, the light is vertically incident on the photon sieve. To ignore the complexity of the incident light, we define it as a plane wave with uniform amplitude. The photon sieve plane and the focal plane is denoted by the x-y plane and the X–Y plane, respectively. The distance between the two planes q is designed to be the focal length f of the photon sieve. In analogy to the zone plate, at photon sieve, pinholes in the same zone must have a similar focal contribution. These pinholes in the mth zone are designed to be uniformly distributed and of equal radius a_m. The distance from the center of the photon sieve to the center of the mth zone is denoted by r_m, and the coordinates of the center of the nth pinhole in the mth zone are denoted by (x_{mn}, y_{mn}). Therefore, $r_m^2 = x_{mn}^2 + y_{mn}^2$. N_m denotes the number of pinholes in the mth zone.

The work of the pinhole ring model was proposed in Refs. [35,36]. The model is derived repeatedly to ensure the integrality of this paper. According to Refs. [28,29], the optical field of the nth pinhole in the mth zone in the focal plane is

$$U_{mn}(X,Y) = \frac{kA_{mn}a_{mn}^2 q}{H_{mn}^2}\exp[\mathrm{j}k(L_{mn}+H_{mn})]\mathrm{Jinc}\left(\frac{ka_{mn}}{H_{mn}}\rho\right), \tag{1}$$

where A_{mn} is the amplitude of the incident light at the pinhole, k is the wave number in vacuum, j is the imaginary unit, and $\rho = [(X - x_{mn})^2 + (Y - y_{mn})^2]^{1/2}$. Because the amplitude of the incident light is identical at all locations of the photon sieve in this study, A_{mn} is omitted. In the discussion of the optical field in the focal plane, q can be replaced by f. From the mathematical form of the formula, we can see that among all the factors, the exponential term has the largest influence. L_{mn} and H_{mn} in the exponential term are given by

$$L_{mn} = L(x_{mn}, y_{mn}) + \frac{\partial L}{\partial x}(x - x_{mn}) + \frac{\partial L}{\partial y}(y - y_{mn}), \tag{2}$$

$$H_{mn} = \sqrt{q^2 + (X - x_{mn})^2 + (Y - y_{mn})^2}. \tag{3}$$

L is the eikonal from light source to the center of specific pinhole in photon sieve. For plane waves, we only consider H_{mn}, as L_{mn} in

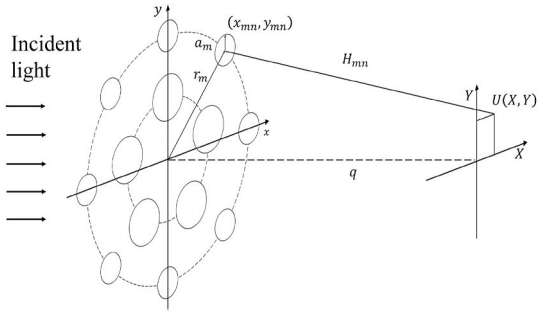

Fig. 1. Schematic view of photon sieve [35]. Reproduction authorized.

Eq. (2) is constant and its influence on the final result is negligible. The Taylor expansion of H_{mn} in Eq. (3) can be written as $H_{mn} \approx f_m + (R^2 - 2x_{mn}X - 2y_{mn}Y)/(2f_m)$, where $f_m^2 = f^2 + r_m^2$ and $R^2 = X^2 + Y^2$. Considering the photon sieve to be circularly symmetrical, the exponential term is converted from rectangular coordinates to polar coordinates. By substituting the Taylor expansion into the exponent, the exponential term can be expressed as

$$\begin{aligned}\exp[\mathrm{j}k(L_{mn}+H_{mn})] &\approx \exp[\mathrm{j}k(f_m-f)]\exp\left(\mathrm{j}k\frac{R^2}{2f_m}\right)\exp\left(-\mathrm{j}k\frac{x_{mn}X+y_{mn}Y}{f_m}\right)\\ &= \exp[\mathrm{j}k(f_m-f)]\exp\left(\mathrm{j}k\frac{R^2}{2f_m}\right)\exp\left[-\mathrm{j}k\frac{r_mR\cos(\varphi-\theta_{mn})}{f_m}\right],\end{aligned} \tag{4}$$

where φ indicates the angular variable in the X–Y plane and θ_{mn} indicates the angle between the x-axis and the line from the original point to the center of the nth pinhole located at the mth zone. Herein, in focusing, phase difference plays a more important role than the phase itself; therefore, we use $\exp[\mathrm{j}k(f_m - f)]$ instead of $\exp(\mathrm{j}kf_m)$ in Eq. (4) as the two expressions are essentially identical.

Because all N_m pinholes are in the mth zone, the optical field in the focal plane can be determined from the arrangement of the pinholes in the photon sieve. Based on the circular symmetry, because the intensity in the center near the focus is much higher than the other positions, the optical field near the focus is considered. Consequently, Eq. (1) simplified considerably, as $X \to 0$, $Y \to 0$, $H_{mn} = f_m$, and $\rho = r_m$. Therefore, the optical field of the pinhole in the focal plane can be written as

$$U_{mn}(X,Y) = \frac{a_m f}{f_m r_m}\exp[\mathrm{j}k(f_m-f)]\exp\left(\mathrm{j}k\frac{R^2}{2f_m}\right)\exp\left[-\mathrm{j}k\frac{r_mR\cos(\varphi-\theta_{mn})}{f_m}\right]\mathrm{J}_1\left(\frac{ka_{mn}}{f_m}r_m\right). \tag{5}$$

As per Eq. (5), for N_m pinholes in the mth zone of the photon sieve, the total optical field is the superposition of the optical fields of the N_m pinholes. The difference between these pinholes is their azimuth angle θ_{mn}; therefore, the sum can be written as

$$\sum_{n=1}^{N_m} U_{mn}(X,Y) = \frac{a_m f}{f_m r_m}\exp[\mathrm{j}k(f_m-f)]\exp\left(\mathrm{j}k\frac{R^2}{2f_m}\right)\mathrm{J}_1\left(\frac{ka_m}{f_m}r_m\right)\sum_{n=1}^{N_m}\exp\left[-\mathrm{j}k\frac{r_mR\cos(\varphi-\theta_{mn})}{f_m}\right]. \tag{6}$$

We assume that all the pinholes in the same zone are uniformly distributed at the ring and had the same radius. Therefore, the difference between the azimuth angles of the two adjacent pinholes is $\Delta\theta = 2\pi/N_m$. Based on this symmetry, the sum form of Eq. (6) can be transformed into the integral form demonstrated as

$$\begin{aligned}\sum_{n=1}^{N_m}\exp\left[-\mathrm{j}k\frac{r_mR\cos(\varphi-\theta_{mn})}{f_m}\right] &= \frac{1}{\Delta\theta}\sum_{n=1}^{N_m}\exp\left[-\mathrm{j}k\frac{r_mR\cos(\varphi-\theta_{mn})}{f_m}\right]\Delta\theta\\ &\approx \frac{1}{\Delta\theta}\int_0^{2\pi}\exp\left[-\mathrm{j}\frac{kRr_m}{f_m}\cos(\varphi-\theta_{mn})\right]\mathrm{d}\theta = N_m\mathrm{J}_0\left(\frac{kRr_m}{f_m}\right).\end{aligned} \tag{7}$$

It should be noted that in this step, the validity of Eq. (7) has certain requirements regarding the number of pinholes. As fewer pinholes affect the accuracy of the function, we recommend at least 20 pinholes in each zone to ensure symmetry.

Thus far, we have obtained a pinhole ring model of the photon sieve. According to this model, the optical field at the focal plane of the whole photon sieve is given by:

$$U(X,Y) = \sum_{m=1}^{M}\sum_{n=1}^{N_m}U_{mn}(X,Y) = \sum_{m=1}^{M}N_m\frac{a_m f}{f_m r_m}\exp[\mathrm{j}k(f_m-f)]\exp\left(\mathrm{j}k\frac{R^2}{2f_m}\right)\mathrm{J}_1\left(\frac{ka_m r_m}{f_m}\right)\mathrm{J}_0\left(\frac{kRr_m}{f_m}\right). \tag{8}$$

To further deduce the model, the photon sieve is divided into M regions, and Eq. (8) is changed to

$$U(X,Y) = \sum_{m=1}^{M}N_m\frac{a_m f}{f_m r_m D_m}\exp[\mathrm{j}k(f_m-f)]\exp\left(\mathrm{j}k\frac{R^2}{2f_m}\right)\mathrm{J}_1\left(\frac{ka_m r_m}{f_m}\right)\mathrm{J}_0\left(\frac{kRr_m}{f_m}\right)D_m, \tag{9}$$

because these two equations are numerically identical. In this case, each region contained one pinhole ring. Let $s = r^2$, and D_m be the width of the mth region in the s coordinate. Therefore, we obtain $\sum_{m=1}^{M} D_m = A^2$, where A represents the radius of the photon sieve. Based on the zone plate theory, $D_m \approx 2\lambda f_m$, f_m only varies slightly, therefore it can be assumed to be uniformly distributed in the s coordinate.

When M is sufficiently large, the sum of Eq. (9) can be reduced to an integral. In addition, in Eq. (9), $D_m \approx ds = 2rdr$. Therefore, the integral can be written as

$$U(X,Y) = \int_0^A N_m\frac{2a_m f}{f_m r_m D_m}\exp[\mathrm{j}k(f_m-f)]\exp\left(\mathrm{j}k\frac{R^2}{2f_m}\right)\mathrm{J}_1\left(\frac{ka_m r_m}{f_m}\right)\mathrm{J}_0\left(\frac{kRr_m}{f_m}\right)r\mathrm{d}r. \tag{10}$$

According to the identical equation of Fourier transform in polar coordinates, $U(R) = 2\pi\int_0^\infty rG(r)\mathrm{J}_0(2\pi rR)\mathrm{d}r$, we obtain Eq. (11) from Eq. (10).

$$U(R) = \exp\left(\mathrm{j}k\frac{R^2}{2F}\right)\frac{2\pi}{\lambda F}\int_0^A N_m\frac{a_m f\lambda F}{\pi f_m r_m D_m}\exp[\mathrm{j}k(f_m-f)]\mathrm{J}_1\left(\frac{ka_m r_m}{f_m}\right)\mathrm{J}_0\left(2\pi\frac{R}{\lambda F}r\right)r\mathrm{d}r. \tag{11}$$

The factor F in Eq. (11) is the average value of all terms of f_m; therefore, it can be simply set as $(f_1 + f_M)/2$. Factor r_m in $J_0(.)$ term in Eq. (11) can be changed to a variable r. The form of Eq. (11) is similar to the Fourier form of the lens-focusing formula. The equivalent pupil function is given by

$$G(r) = \begin{cases} G(r_m), 0 \le r \le A \\ 0, r > A \end{cases}, \\ G(r_m) = N_m \frac{a_m f \lambda F}{\pi f_m r_m D_m} \exp[\mathrm{j}k(f_m - f)] \mathrm{J}_1\left(\frac{k a_m r_m}{f_m}\right). \tag{12}$$

As the size of a real optical element is finite, its pupil function would be truncated at the boundary.

Based on the pinhole ring model, we have established the transformation relation between the photon sieve plane and focal plane. $G(r)$ represents the equivalent pupil function, which is truncated in a real optical element; it is $G(r_m)$ when the radius in the range of $0 \le r \le A$ and zero when the radius is greater than A. Using Eq. (12), we can observe the effect of the pinhole parameters on the value of the equivalent pupil function. The position, size, and number of pinholes can affect the contribution of the focal spot. Therefore, similar to the formula in Refs. [43,44] for designing zone plate, by regulating the parameters of the pinholes, we can adjust the equivalent pupil function and modulate the final field distribution of the focal spot of the photon sieve.

3. Flattened Gaussian beams with uniform phase

The flattened Gaussian beam, proposed by Gori in 1994 [9], has attracted considerable attention. As shown in Eq. (13), Gori expanded $\exp(-\pi R^2)$ using the Taylor expansion, took its first n terms, and multiplied it by the Gaussian function. As Gaussian functions decay faster than polynomials, a flat-top function can be easily obtained.

$$\sum_{n=0}^{\infty} \frac{(\pi R^2)^n}{n!} e^{-\pi R^2} = 1. \tag{13}$$

The $\exp(-\pi r^2)$ and $\exp(-\pi R^2)$ are basic Fourier transform pairs. Once the functional form of the optical field in the focal plane is determined, we can find the pupil function by inverse Fourier transform. The core of this problem is the inverse Fourier transform of $(\pi R^2)^n \exp(-\pi R^2)$. To facilitate the operation, we use a rectangular coordinate system at first.

$$U(x, y) = \iint \exp\left(-\pi X^2\right) \exp\left(-\pi Y^2\right) \exp[\mathrm{j}2\pi(Xx + Yy)] \mathrm{d}X\mathrm{d}Y. \tag{14}$$

Next, we set up a Fourier transform, as displayed in Eq. (14). The Laplace operator of $U(x, y)$ is the Fourier transform of the function $(\pi R^2)\exp(-\pi R^2)$, as displayed in Eq. (15). Therefore, by proceeding with the Laplace operator, we obtain the Fourier transform of the function $(\pi R^2)^n \exp(-\pi R^2)$.

$$\nabla^2 U(x, y) = -4\pi^2 \iint \left(X^2 + Y^2\right) \exp\left(-\pi X^2\right) \exp\left(-\pi Y^2\right) \exp[\mathrm{j}2\pi(Xx + Yy)] \mathrm{d}X\mathrm{d}Y. \tag{15}$$

To make the function computable, we perform some variation on the left side of Eq. (15). By letting $v = -\pi r^2$ and expanding the Laplace operator into polynomials, we obtain $\nabla^2 e^v = e^v(v + 1)$, $(\nabla^2)^2 e^v = e^v(v^2 + 4v + 2)$, and $(\nabla^2)^3 e^v = e^v(v^3 + 9v^2 + 18v + 6)$. As expected, these polynomials obey the form of Laguerre polynomials. However, it is not adopted as the general formula of the Laguerre polynomials is substantially complicated. It can be seen that the order of variable v in the polynomials increases as the Laplace operator order increases. We represent $(\nabla^2)^n e^v$ as $e^v \sum_{m=0}^{n} C_{n,m} v^m$. Therefore, $(\nabla^2)^{n-1} e^v$ can be written as $e^v \sum_{m=0}^{n-1} C_{n-1,m} v^m$. For $(\nabla^2)^n e^v = \nabla^2[(\nabla^2)^{n-1} e^v]$, $e^v \sum_{m=0}^{n} C_{n,m} v^m = \nabla^2[e^v \sum_{m=0}^{n-1} C_{n-1,m} v^m]$ is natural. The Laplace operator for e^v in *the* v coordinate is as follows:

$$\nabla^2 = (-4\pi) \frac{d}{dv}\left(v \frac{d}{dv}\right). \tag{16}$$

Initially, the constant factor -4π is not considered, and the recurrence relation is expressed as follows:

$$e^v \sum_{m=0}^{n} C_{n,m} v^m = e^v \left[\sum_{m=0}^{n-1} C_{n-1,m} v^{m+1} + \sum_{m=0}^{n-1} (2m+1) C_{n-1,m} v^m + \sum_{m=0}^{n-1} m^2 C_{n-1,m} v^{m-1}\right]. \tag{17}$$

Subsequently, the coefficients in Eq. (17) attain a matrix form. The factors in $(\nabla^2)^n e^v$ and $(\nabla^2)^{n-1} e^v$ are expressed by sequence separately, and the relationship between them is T, which is the below given matrix. Here, by taking the constant factor -4π into account, we can get $(\nabla^2)^n e^v = (-4\pi)^n e^v V_n T^n P_0$. In this formula, $V_n = [v^n\ v^{n-1}\ v^{n-2}\ v^{n-3}\ v^{n-4} \cdots v^4\ v^3\ v^2\ v\ 1]$, and $P_0 = [0\ 0\ 0\ 0\ 0 \cdots 0\ 0\ 0\ 0\ 1]^{\mathrm{T}}$.

$$T=\begin{bmatrix} 2n+1 & 1 & 0 & 0 & 0 & \cdots & 0 & 0 & 0 & 0 & 0 \\ n^2 & 2n-1 & 1 & 0 & 0 & \cdots & 0 & 0 & 0 & 0 & 0 \\ 0 & (n-1)^2 & 2n-3 & 1 & 0 & \cdots & 0 & 0 & 0 & 0 & 0 \\ 0 & 0 & (n-2)^2 & 2n-5 & 1 & \cdots & 0 & 0 & 0 & 0 & 0 \\ 0 & 0 & 0 & (n-3)^2 & 2n-7 & \cdots & 0 & 0 & 0 & 0 & 0 \\ \vdots & \vdots & \vdots & \vdots & \vdots & \ddots & \vdots & \vdots & \vdots & \vdots & \vdots \\ 0 & 0 & 0 & 0 & 0 & \cdots & 9 & 1 & 0 & 0 & 0 \\ 0 & 0 & 0 & 0 & 0 & \cdots & 16 & 7 & 1 & 0 & 0 \\ 0 & 0 & 0 & 0 & 0 & \cdots & 0 & 9 & 5 & 1 & 0 \\ 0 & 0 & 0 & 0 & 0 & \cdots & 0 & 0 & 4 & 3 & 1 \\ 0 & 0 & 0 & 0 & 0 & \cdots & 0 & 0 & 0 & 1 & 1 \end{bmatrix}. \tag{18}$$

Taking all the equations in this section into account, we can obtain the Fourier transform relationship of the flattened Gaussian function as

$$e^{-\pi r^2}\sum_{l=0}^{n}\frac{V_l T^l P_0}{l!}=\mathscr{F}^{-1}\left\{e^{-\pi R^2}\sum_{l=0}^{n}\frac{(\pi R)^l}{l!}\right\}. \tag{19}$$

The flattened Gaussian focal spot form of Eq. (19) can be obtained by representing the left side of the equation as the equivalent pupil function (details in Appendix A), and the right side of the equation as the parameters of the focal spot. The integer n in Eq. (19) indicates the order of the flattened Gaussian function. To analytically present this Fourier transform relationship, phase information can also be included when the specific parameters are satisfied. As a result, we can obtain a flat-top Gaussian beam with a uniform phase.

4. Numerical simulation

Based on the above model, we designed a photon sieve that works in the soft X-ray band. Soft X-ray can be absorbed by other organic molecules of the organism in the water window band of 2.4–4.5 nm, where the water is transparent. The light in this band can be used for biological imaging. The working wavelength, focal length, and the total radius of the photon sieve were set to be 3 nm, 1 mm, and 50 μm, respectively. We set these parameters to demonstrate the simulation; for the actual element, all these parameters can be changed as per requirement. According to Eq. (19), we took the sum of the first nine terms of the Taylor expansion to obtain the 9-order flattened Gaussian beam in the focal plane; the focal spot of the 9-order was found to be better than that of the 8- or 10-order; this may be due to the truncation of the equivalent pupil function.

First, we calculated the equivalent pupil function of the photon sieve. Fig. 2 displays the normalized 9-order flattened Gaussian function and the corresponding equivalent pupil function in the polar coordinate direction, which are the Fourier transforms of each other. Although the flattened Gaussian function and the equivalent pupil function are infinitely extended in the plane, the radius of the photon sieve is finite. Therefore, the equivalent pupil function had to be truncated. In the simulation, a quick calculation was performed to determine that the designed photon sieve can have 416 zones, and 400 rings were picked up for truncation. Based on the design of the photon sieve, the value of the equivalent pupil function can be positive or negative. When the value was positive, the center of the pinhole was located in the bright ring zone, whereas when the value was negative, it was located in the dark ring zone. When the value approached zero, we could control the size of the pinhole so that its contribution to the optical field approached zero as well. A related discussion was presented in Refs. [29,43,44].

To test the accuracy of the equivalent pupil function model, two computational methods were used to simulate the optical field at the focal plane of the photon sieve, namely the non-paraxial pinhole and the pinhole ring models. The non-paraxial pinhole model needs to calculate the optical field superposition of all pinholes in the focal plane of the photon sieve; in addition, the photon sieve

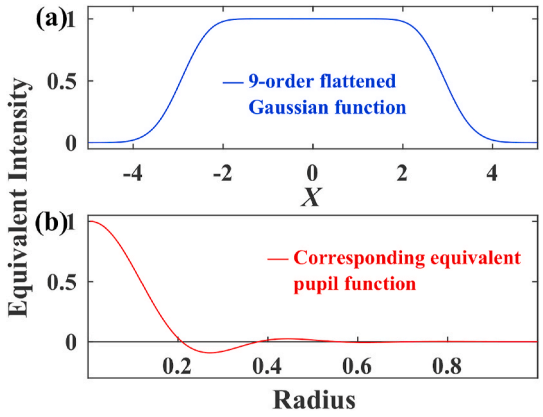

Fig. 2. (a) 9-order flattened Gaussian function. (b) The corresponding equivalent pupil function.

needs to be designed in advance. Consequently, the non-paraxial pinhole model requires more computational time. In contrast, because the pinhole ring model (or the equivalent pupil function model) treats all the pinholes in one zone as a ring, it only needs to design the equivalent pupil function and does not require a complete photon sieve, thereby allowing faster calculations.

Then, we simulated the pinhole ring model. In this model, the curve in Fig. 2(b) was truncated and sampled as coefficients. We multiplied every coefficient and the diffraction integral of the corresponding ring in the zone plate, and summed these products to get the result. The radial intensity distribution and phase distribution of the optical field in the focal plane are displayed in Fig. 3. The intensity in the central region was very high and nearly identical. As displayed in Fig. 3(a), the nonuniformity of the beam was close to 1% in the circular region within a radius of 100 nm. After a displacement away from the center, the light intensity decreased as a Gaussian function. It should be emphasized that in the central region of high intensity, as demonstrated in Fig. 3(b), the phase was uniform as well. Within this region, the phase difference did not exceed 1/170 wavelength. When the light intensity dropped to near zero, a phase change occurred. However, since the light intensity was already negligible at these places, the phase change did not affect the overall light spot. By comparing the curves in Figs. 2(a) and Fig. 3(a), we confirmed that the designed focal spot conforms to the expectation.

Herein, we can determine the specific parameters of the optical field through the Fourier transform relation between the equivalent pupil function and the optical field distribution in the focal plane. In addition, we can exchange the sequence and design the optical field first in the other scheme. Consequently, there is no need to design the whole photon sieve, which saves considerable time.

Once the Fourier transform pair has been determined, the photon sieve can be designed. We had to determine the location, number, and size of the pinholes in the photon sieve. A schematic view of the designed photon sieve of the 9-order flattened Gaussian focal spot is displayed in Fig. 4. At the center of the photon sieve, because the value of the equivalent pupil function was positive, the pinholes occupied most of the area of the zone. When the value of the equivalent pupil function decreased, the diameter and number of pinholes decreased as well. When the value of the equivalent pupil function approached zero, we chose a suitable diameter and number of pinholes to ensure manufacturability and symmetry. Although only one design scheme has been displayed here, there could be various other schemes. As long as the overall focusing contribution of each ring meets the requirements, the design requirements of a single pinhole can be regulated appropriately.

The photon sieve designed as per the schematic in Fig. 4 was simulated for the non-paraxial pinhole model, which is closer to reality than the equivalent pupil function model. The simulation results are presented in Fig. 5. As per Fig. 5(a), the nonuniformity in the intensity of the optical field was still less than 2%. As per Fig. 5(b), the phase change of the focal spot center was less than 1/1496 wavelength. In the central region of the uniform focal spot intensity, the phase was uniform as well. Comparing Fig. 3 with Fig. 5, it can be seen that the curves in the figures were very close to the other, and the phase changes occurred in a similar position as well. In addition, the phase curve in Fig. 5(b) changed slightly slower than that in Fig. 3(b). These results suggest that the equivalent pupil function model exhibited similar performance to that of the traditional model. In addition, it worked well in the simulation of photon sieve.

To explain the phase change, we further compared the intensity of the two models shown in Figs. 3 and 5 in the log scale. As shown in Fig. 6, the intensity distributions of the two models in Fig. 6(a) are the same, and the phase distributions in Fig. 6(b) are slightly different. It can be seen that the phase of the ideal model changes more sharply than that of the real model. The difference comes from the fact that two-dimensional simulations are closer to reality than one-dimensional ones. The phase changed rapidly from zero to π when the intensity approached zero, indicating the presence of a node in the focal light field, which suggested a sidelobe. Theoretically, the flattened Gaussian function does not have a node or sidelobe. The equivalent pupil function is truncated due to the limited size of photon sieve, the sidelobe appears in the designed flattened Gaussian beam.

To show the advantages of the produced flattened Gaussian beam, we compare them with the normal Gaussian beam. As shown in

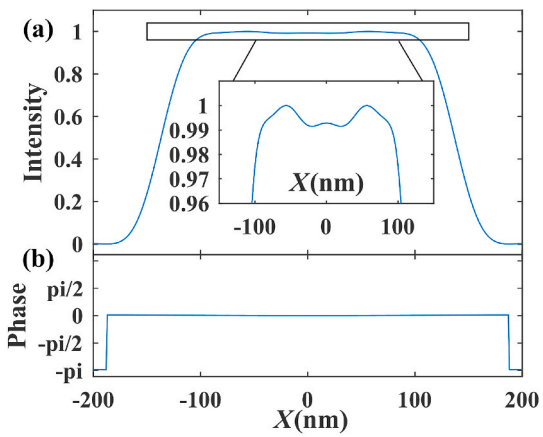

Fig. 3. Simulation results of the equivalent pupil function model. (a) Intensity of the focal spot in *X*–*Y* plane; inset: top area of the intensity. The nonuniformity of the focal spot was approximately 1%. (b) Phase of the focal spot in *X*–*Y* plane. The phase was primarily stable in the focal area and changed sign when the intensity became zero.

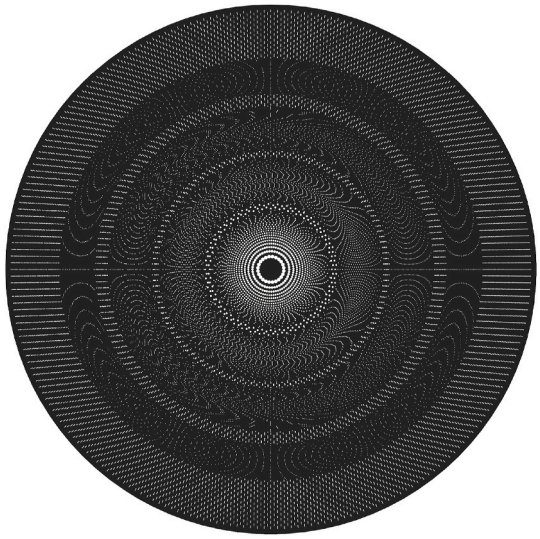

Fig. 4. Schematic view of designed photon sieve that produced 9-order flattened Gaussian optical field.

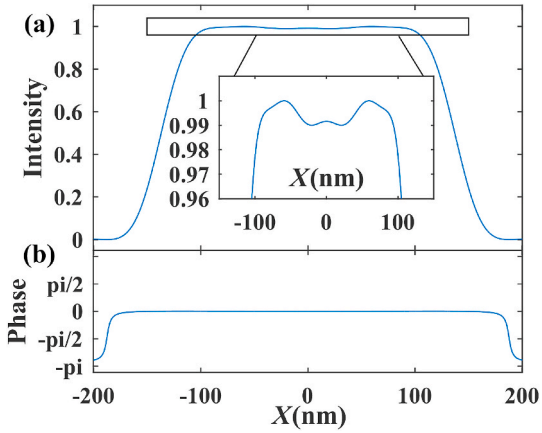

Fig. 5. Simulation results of the non-paraxial pinhole model of designed photon sieve. (a) Intensity of the focal spot in *X*–*Y* plane; the inset indicates that the nonuniformity of the focal spot was approximately 1%. (b) Phase of the focal spot in *X*–*Y* plane; the phase change was below 1/1496 wavelength in the focal area.

Fig. 7, the spot size (FWHM) of the flattened Gaussian beam is 274 nm, while that of the normal Gaussian beam is 58 nm, and the difference in spot size between these two kinds of beams is 4.7 times. Their transverse resolution is 189 nm and 108 nm, respectively. Both of the sidelobes are very small, and the normalized intensities of sidelobes are less than 0.01, which are almost negligible. The total diffraction efficiency of the designed photon sieve that generates the flattened Gaussian beam is 0.12%, and the diffraction efficiency of the normal Gaussian beam is 0.68%.

We also simulate the transverse distribution of the designed photon sieve. As shown in Fig. 8, the photon sieve has the largest focal spot at the focal length, and its axial size is 0.1 mm. Due to the special equivalent pupil function and symmetry of the designed photon sieve, focal spots of even-order diffraction can also appear. By comparison, we can see that the flattened Gaussian beam has obvious advantages over the usual Gaussian beam in uniform illumination.

The numerical simulations in this section have demonstrated the following points: (1) the equivalent pupil function model was effective, and (2) the flattened Gaussian focal spot produced by this photon sieve exhibited a highly uniform degree of intensity and phase. The produced optical field has great potential for application in biological imaging for illuminating specimens and other associated fields.

Because the light field distribution on the focal plane depends on the equivalent pupil function of the photon sieve, numerical accuracy is very important in this theory. At the same time, the symmetry of the pinholes of the photon sieve is necessary to ensure the uniformity of the light field. Compared with the two-dimensional Fourier transform [45], our approach is to take the one-dimensional Fourier–Bessel transform of the radial coordinate *r*, which is theoretically faster than the two-dimensional Fourier transform of the *x*-*y* coordinate.

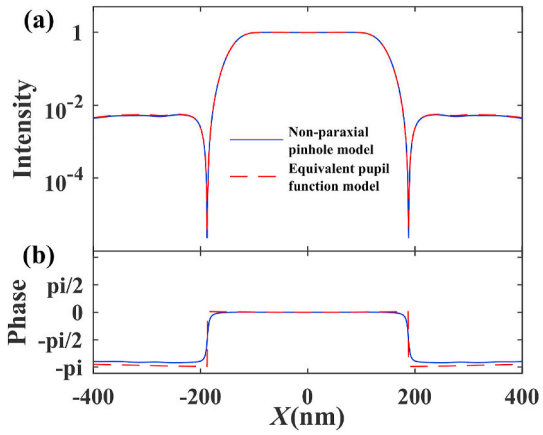

Fig. 6. Intensity and phase distribution of designed photon sieve simulated by the non-paraxial pinhole model (blue line) and the equivalent pupil function model (red dash line). (a) Intensity distribution (in log scale), and (b) phase distribution. (For interpretation of the references to colour in this figure legend, the reader is referred to the Web version of this article.)

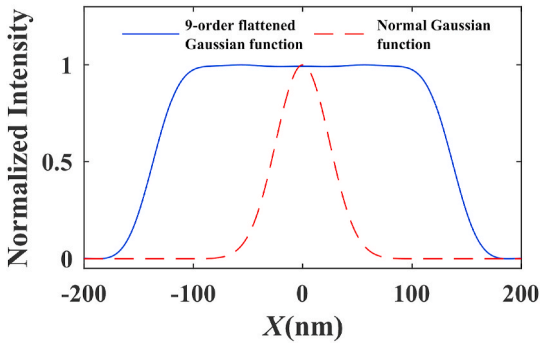

Fig. 7. Calculated intensity distributions of the flattened Gaussian function (blue line), and the normal Gaussian function (red dash line). The focal spot sizes (FWHM) are 274 nm and 58 nm. The transverse resolutions are 189 nm and 108 nm, respectively. (For interpretation of the references to colour in this figure legend, the reader is referred to the Web version of this article.)

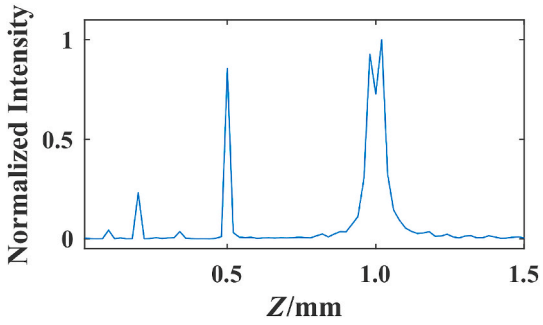

Fig. 8. Longitudinal intensity distribution of the designed photon sieve. The axial focal spot size is 0.1 mm.

Meanwhile, there are also constraints for fabricating the device. The imaging theory of photon sieve depends on optical path differences. The most important part of fabricating a photon sieve is to locate the position of pinholes. Large deviations in positioning may bring about large errors. Since this theory involves quantitative calculation, precise control of pinhole size should also be considered. Fortunately, deviations in the same ring can be compensated by each other to some extent. For the purpose of uniform illumination, the current machining accuracy of about 2 nm should be enough [15].

5. Conclusion

In summary, based on the pinhole ring model of the photon sieve, we have established the equivalent pupil function theory for a rotating symmetric photon sieve and derived the equivalent pupil function expression for a flattened Gaussian focal spot with a uniform phase produced by the photon sieve. In addition, we have analytically derived the inverse Fourier transform of the flattened Gaussian function. Based on the equivalent pupil function expression, we have designed a photon sieve scheme that works in the water window band of soft X-ray and evaluated it using numerical simulation. As per the results, the focal spot intensity nonuniformity in the focal plane was close to 1%, and the phase change was less than 1/170 wavelength. This work can be utilized to design different types of photon sieves that can produce a flattened Gaussian focal spot with uniform phase, thereby providing a new scheme and idea for uniform illumination in biological imaging. In addition, it lays a foundation for the application of a flattened Gaussian beam with a uniform phase.

Author contribution statement

Changjie Cheng: Conceived and designed the experiments; Performed the experiments; Analyzed and interpreted the data; Contributed reagents, materials, analysis tools or data; Wrote the paper.

Qing Cao: Conceived and designed the experiments; Performed the experiments; Analyzed and interpreted the data; Contributed reagents, materials, analysis tools or data.

Lihua Bai, Chaoyue Li, Jirui Zhu: Performed the experiments; Contributed reagents, materials, analysis tools or data.

Data availability statement

Data will be made available on request.

Funding

This research did not receive any specific grant from funding agencies in the public, commercial, or not-for-profit sectors.

Declaration of competing interest

The authors declare that they have no known competing financial interests or personal relationships that could have appeared to influence the work reported in this paper.

Acknowledgments

The authors thank Dr. Da Teng and Dr. Hua Gao for inspiring discussions and help with the program.

Appendix A

Generally, there are two parallel planes denoted by the x-y plane and the X–Y plane, respectively. The function $F(X, Y)$ in the X–Y plane is the Fourier transform of the function $f(x, y)$ in the x-y plane, which can be written as $F(X, Y) = \mathscr{F}\{f(x, y)\}$ or $f(x, y) = \mathscr{F}^{-1}\{F(X, Y)\}$.

In this article, the flattened Gaussian beam is the desired profile, so the function in the X–Y plane is

$$F(X, Y) = \sum_{n=0}^{\infty} \frac{(\pi R^2)^n}{n!} e^{-\pi R^2}. \tag{A.1}$$

From Eq. (14) and Eq. (15), we can derive the relation $\mathscr{F}^{-1}\{-4\pi(\pi R^2)\exp(-\pi R^2)\} = \nabla^2[\exp(-\pi r^2)]$ and $\mathscr{F}^{-1}\{(-4\pi)^n(\pi R^2)^n\exp(-\pi R^2)\} = (\nabla^2)^n[\exp(-\pi r^2)]$. From this relation, we can know

$$f(x, y) = \sum_{n=0}^{\infty} \frac{(\nabla^2)^n[\exp(-\pi r^2)]}{n!(-4\pi)^n}. \tag{A.2}$$

Because the Laplace operator in this equation is not intuitive for calculation, we transformed the Laplace operator to polynomials first and to matrix form then. From Eq. (16) to Eq. (18), we simplified the Laplace operator as $(\nabla^2)^n e^{\nu} = (-4\pi)^n e^{\nu} V_n T^n P_0$. In this formula, $\nu = -\pi r^2$, $V_n = [\nu^n\ \nu^{n-1}\ \nu^{n-2}\ \nu^{n-3}\ \nu^{n-4} \cdots \nu^4\ \nu^3\ \nu^2\ \nu\ 1]$, and $P_0 = [0\ 0\ 0\ 0\ 0 \cdots 0\ 0\ 0\ 0\ 1]^{\mathrm{T}}$. Combining this formula with Eq. (A.2), we can get

$$f(x, y) = \sum_{n=0}^{\infty} \frac{\exp(-\pi r^2) V_n T^n P_0}{n!}. \tag{A.3}$$

According to Eq. (A.1) and Eq. (A.3), the Fourier transform relation of two planes for a certain order flattened Gaussian beam can be established, it was written as Eq. (19).

Let us return to Eq. (11). This expression is obviously a form of Fourier transform. These two Fourier transforms of Eq. (11) and Eq. (19) can be combined to design a photon sieve which can produce flattened Gaussian focal spot. For example, we can calculate a curve just like Fig. 2(b) from Eq. (19). Then, curve is sampled for Eq. (12) to set the photon sieve parameters. Wavelength λ and focal length f should be determined first for a certain situation, thus r_m and D_m are subsequently determined according to the zone plate theory. So, we only need to decide the radius a_m and amount of pinholes N_m in the mth ring. Putting N_m the aside, we can find the $G(r_m)$ in Eq. (12) is similar to the widely used curve of d/w ≈ 1.5, 3.5, 5.5, …in Ref. [29]. The rest for us to do is to fit the product of this curve and N_m to Fig. 2(b), so that we can get the value of a_m and N_m for each ring.

References

[1] M. Born, E. Wolf, Principles of Optics: Electromagnetic Theory of Propagation, Interference and Diffraction of Light, Cambridge University, London, 1999, pp. 598–599.
[2] G. Denbeaux, L. Johnson, W. Meyer-Ilse, Spectromicroscopy at the XM-1, AIP Conf. Proc. 507 (2000) 478–483, https://doi.org/10.1063/1.1291194.
[3] A. Mau, K. Friedl, C. Leterrier, N. Bourg, S. Leveque-Fort, Fast widefield scan provides tunable and uniform illumination optimizing super-resolution microscopy on large fields, Nat. Commun. 12 (2021) 11, https://doi.org/10.1038/s41467-021-23405-4.
[4] M. Chen, Y. Wang, A.J. Zeng, J. Zhu, B.X. Yang, H.J. Huang, Flat Gauss illumination for the step-and-scan lithographic system, Opt Commun. 372 (2016) 201–209, https://doi.org/10.1016/j.optcom.2016.04.033.
[5] X. Deng, X. Liang, Z. Chen, W. Yu, R. Ma, Uniform illumination of large targets using a lens array, Appl. Opt. 25 (3) (1986) 377–381, https://doi.org/10.1364/AO.25.000377.
[6] O. Homburg, D. Hauschild, F. Kubacki, V. Lissotschenko, Efficient beam shaping for high-power laser applications, Proc. SPIE 6216 (2006), 621608, https://doi.org/10.1117/12.668004.
[7] T. Hirvonen, J.P. S Ala-Laurinaho, J. Tuovinen, A.V. Raisanen, A compact antenna test range based on a hologram, IEEE Trans. Antenn. Propag. 45 (8) (1997) 1270–1276, https://doi.org/10.1109/8.611247.
[8] D.N. Gupta, A. Jain, V.V. Kulagin, M.S. Hur, H. Suk, Coherent terahertz radiation generation by a flattened Gaussian laser beam at a plasma–vacuum interface, Appl. Phys. B 128 (3) (2022) 1–9, https://doi.org/10.1007/s00340-022-07777-z.
[9] F. Gori, Flattened Gaussian beams, Opt. Commun. 107 (5–6) (1994) 335–341, https://doi.org/10.1016/0030-4018(94)90342-5.
[10] V. Bagini, R. Borghi, F. Gori, A.M. Pacileo, M. Santarsiero, D. Ambrosini, G.S. Spagnolo, Propagation of axially symmetric flattened Gaussian beams, J. Opt. Soc. Am. A 13 (7) (1996) 1385–1394, https://doi.org/10.1364/JOSAA.13.001385.
[11] M. Santarsiero, D. Aiello, R. Borghi, S. Vicalvi, Focusing of axially symmetric flattened Gaussian beams, J. Mod. Opt. 44 (3) (1997) 633–650, https://doi.org/10.1080/09500349708232927.
[12] M. Shen, S. Wang, D. Zhao, Propagation of flattened Gaussian beams passing through a misaligned optical system with finite aperture, Optik 115 (5) (2004) 193–196, https://doi.org/10.1078/0030-4026-00346.
[13] C. Palma, V. Bagini, Propagation of super-Gaussian beams, Opt. Commun. 111 (1–2) (1994) 6–10, https://doi.org/10.1016/0030-4018(94)90130-9.
[14] C.J.R. Sheppard, S. Saghafi, Flattened light beams, Opt. Commun. 132 (1–2) (1996) 144–152, https://doi.org/10.1016/0030-4018(96)00310-0.
[15] L. Kipp, M. Skibowski, R.L. Johnson, R. Berndt, R. Adelung, S. Harm, R. Seemann, Sharper images by focusing soft X-rays with photon sieves, Nature 414 (2001) 184–188, https://doi.org/10.1038/35102526.
[16] F. Giménez, J.A. Monsoriu, W.D. Furlan, A. Pons, Fractal photon sieve, Opt. Exp. 14 (25) (2006) 11958–11963, https://doi.org/10.1364/oe.14.011958.
[17] C. Xie, X. Zhu, L. Shi, M. Liu, Spiral photon sieves apodized by digital prolate spheroidal window for the generation of hard-X-ray vortex, Opt. Lett. 35 (11) (2010) 1765–1767, https://doi.org/10.1364/ol.35.001765.
[18] C. Hou, Novel diffractive optical element: binary photon sieve, Opt. Eng. 50 (2011) 4, https://doi.org/10.1117/1.3589294.
[19] Y. Li, C. Wang, X. Zhao, F. Xu, C. Wang, Multispectral and large bandwidth achromatic imaging with a single diffractive photon sieve, Opt. Exp. 26 (16) (2018) 21141–21152, https://doi.org/10.1364/oe.26.021141.
[20] K. Huang, H. Liu, F.J. Garcia-Vidal, M.H. Hong, B. Luk'yanchuk, J.H. Teng, C.W. Qiu, Ultrahigh-capacity non-periodic photon sieves operating in visible light, Nat. Commun. 6 (2015) 7, https://doi.org/10.1038/ncomms8059.
[21] G. Andersen, Large optical photon sieve, Opt. Lett. 30 (22) (2005) 2976–2978, https://doi.org/10.1364/ol.30.002976.
[22] G. Andersen, Membrane photon sieve telescopes, Appl. Opt. 49 (33) (2010) 6391–6394, https://doi.org/10.1364/ao.49.006391.
[23] Y. Li, H. Liu, J. Xie, J. Zhang, Radial-shearing interferometric imaging with Theon-Kepler bifocal telescope, Appl. Opt. 59 (17) (2020) 5265–5268, https://doi.org/10.1364/ao.392574.
[24] Y. Cheng, J. Tong, J. Zhu, J. Liu, S. Hu, Y. He, Clad photon sieve for generating localized hollow beams, Opt. Laser. Eng. 77 (2016) 18–25, https://doi.org/10.1016/j.optlaseng.2015.07.003.
[25] A.Ö. Yöntem, J. Li, D. Chu, Imaging through a projection screen using bi-stable switchable diffusive photon sieves, Opt. Exp. 26 (8) (2018) 10162–10170, https://doi.org/10.1364/oe.26.010162.
[26] K. Huang, H. Liu, G. Si, Q. Wang, J. Lin, J. Teng, Photon-nanosieve for ultrabroadband and large-angle-of-view holograms, Laser Photon. Rev. 11 (3) (2017), 1700025, https://doi.org/10.1002/lpor.201700025.
[27] J. Zhang, Z. Ren, J. Zhu, Z. Lin, Phase-shifting lensless Fourier-transform holography with a Chinese Taiji lens, Opt. Lett. 43 (17) (2018) 4085–4087, https://doi.org/10.1364/ol.43.004085.
[28] W.D. Furlan, S. García-Delpech, P. Udaondo, L. Remón, V. Ferrando, J.A. Monsoriu, Diffractive corneal inlay for presbyopia, J. Biophot. 10 (9) (2017) 1110–1114, https://doi.org/10.1002/jbio.201600320.
[29] Q. Cao, J. Jahns, Focusing analysis of the pinhole photon sieve: individual far-field model, J. Opt. Soc. Am. A 19 (12) (2002) 2387–2393, https://doi.org/10.1364/josaa.19.002387.
[30] Q. Cao, J. Jahns, Nonparaxial model for the focusing of high-numerical-aperture photon sieves, J. Opt. Soc. Am. A 20 (6) (2003) 1005–1012, https://doi.org/10.1364/josaa.20.001005.
[31] J. Zhang, Q. Cao, X. Lu, Z. Lin, Individual far-field model for photon sieves composed of square pinholes, J. Opt. Soc. Am. A 27 (6) (2010) 1342–1346, https://doi.org/10.1364/josaa.27.001342.
[32] Y. Liu, X. Zhu, Y. Gao, W. Zhang, Q. Fan, L. Wei, Z. Yang, Q. Zhang, F. Qian, Y. Chen, W. He, Y. Wu, Z. Yan, Y. Hua, Y. Zhao, M. Cui, R. Qiu, W. Zhou, Y. Gu, B. Zhang, C. Xie, L. Cao, Quasi suppression of higher-order diffractions with inclined rectangular apertures gratings, Sci. Rep. 5 (2015), 16502, https://doi.org/10.1038/srep16502.
[33] T. Pu, Z. Liu, L. Shi, G. Wang, J. Niu, C. Xie, Effects of structure parameters on high-order diffraction suppression of quasi-periodic gratings, J. Opt. Soc. Am. B 35 (4) (2018) 711–717, https://doi.org/10.1364/josab.35.000711.
[34] F.S. Oktem, F. Kamalabadi, J.M. Davila, Analytical Fresnel imaging models for photon sieves, Opt Express 26 (24) (2018) 32259–32279, https://doi.org/10.1364/oe.26.032259.
[35] T. Liu, X. Zhang, L. Wang, Y. Wu, J. Zhang, H. Qu, Fast and accurate focusing analysis of large photon sieve using pinhole ring diffraction model, Appl. Opt. 54 (17) (2015) 5327–5331, https://doi.org/10.1364/ao.54.005327.

[36] T. Liu, L. Wang, J. Zhang, Q. Fu, X. Zhang, Numerical simulation and design of an apodized diffractive optical element composed of open-ring zones and pinholes, Appl. Opt. 57 (1) (2018) 25–32, https://doi.org/10.1364/ao.57.000025.
[37] H. Zang, S. Ding, L. Wei, C. Wang, Q. Fan, L. Cao, Fractal spiral zone plate with high-order harmonics suppression, Appl. Opt. 58 (31) (2019) 8680–8686, https://doi.org/10.1364/ao.58.008680.
[38] A. Sabatyan, S. Jaafari, P. Roshaninejad, K. Aghadoost, Focusing and imaging properties of a dense Gaussian apodized photon sieve, Opt Commun. 310 (2014) 42–47, https://doi.org/10.1016/j.optcom.2013.07.052.
[39] A. Sabatyan, S. Mirzaie, Efficiency-enhanced photon sieve using Gaussian/overlapping distribution of pinholes, Appl. Opt. 50 (11) (2011) 1517–1522, https://doi.org/10.1364/ao.50.001517.
[40] A. Sabatyan, P. Roshaninejad, Super-resolving random-Gaussian apodized photon sieve, Appl. Opt. 51 (26) (2012) 6315–6318, https://doi.org/10.1364/ao.51.006315.
[41] T. Liu, X. Zhang, L.J. Wang, Y.X. Wu, J.Z. Zhang, H.M. Qu, Multiregion apodized photon sieve with enhanced efficiency and enlarged pinhole sizes, Appl. Opt. 54 (24) (2015) 7175–7180, https://doi.org/10.1364/ao.54.007175.
[42] G.X. Cheng, C. Hu, P. Xu, T.W. Xing, Zernike apodized photon sieves for high-resolution phase-contrast x-ray microscopy, Opt. Lett. 35 (21) (2010) 3610–3612, https://doi.org/10.1364/ol.35.003610.
[43] Q. Cao, J. Jahns, Modified Fresnel zone plates that produce sharp Gaussian focal spots, J. Opt. Soc. Am. A 20 (8) (2003) 1576–1581, https://doi.org/10.1364/josaa.20.001576.
[44] Q. Cao, J. Jahns, Comprehensive focusing analysis of various Fresnel zone plates, J. Opt. Soc. Am. A 21 (4) (2004) 561–571, https://doi.org/10.1364/josaa.21.000561.
[45] S. Ayazgok, F.S. Oktem, Efficient computation of 2D point-spread functions for diffractive lenses, Appl. Opt. 59 (2) (2020) 445–451, https://doi.org/10.1364/ao.59.000445.